East European Journal of Physics. 1. 413-427 (2026)
DOI:10.26565/2312-4334-2026-1-50 ISSN 2312-4334

DEEP LEARNING-BASED MRI DENOISING USING NOISE STATISTICS DERIVED FROM PHYSICAL PHANTOM MEASUREMENTS

D.G. Sliusarenko[1,2]*, A.V. Netreba[1]
[1]*Faculty of Radiophysics, Electronics and Computer Systems, National Taras Shevchenko University of Kyiv, 64/13, Volodymyrska Street, Kyiv, Ukraine, 01601*
[2]*National Cancer Institute of Ukraine, Yulii Zdanovskoi Street, 33/43, Kyiv, Ukraine, 03022*
**Corresponding Author email: d.fulhem@gmail.com*
Received December 21, 2025; revised February 18, 2026; accepted February 20, 2026

High-quality MRI images are essential for accurate definition of target volumes and organs at risk, as well as for correct registration with CT scans when planning radiotherapy. The aim of this work is to develop a robust denoising method that improves visualization of brain structures and preserves anatomical details. A model based on a modified U-Net architecture with residual blocks, attention modules (CBAM) and spatial pyramidal pooling is proposed. The approach is characterized by the integration of statistical noise characteristics obtained from phantom measurements and modeling of degradations in pseudo-k-space (including Gaussian and Rayleigh noise distributions). The validation was performed on 1000 anonymized clinical DICOM images with variable noise levels. The proposed model provided an increase in PSNR by 8–10 dB and an increase in SSIM from 0.72 to 0.97. The edge preservation index (EPI), which reached values of 8.0 on noisy images due to artifacts, stabilized at 1.0 after processing, indicating effective removal of pseudo-contours without blurring true anatomical boundaries. In addition, an average SNR improvement of 7% and a CV reduction of 4–7% were observed on real images, confirming the stability of the method. The combination of physically based noise modeling in the frequency domain and modern deep learning architectures allows for effective noise removal while preserving critical anatomical boundaries. The method has high potential for clinical implementation in radiotherapy planning procedures, in particular to improve the accuracy of MRI/CT fusion.
Keywords: *MRI denoising; k-space noise modeling; Deep learning; Adaptive noise scaling; Fourier domain simulation; Medical image reconstruction; CNN*
PACS: 87.57.N-, 07.05.Mh, 87.61.Tg, 02.50.-r

1. INTRODUCTION

The quality of medical images directly affects the accuracy of diagnosis, the effectiveness of treatment planning and the ability to track the results of therapy. Magnetic resonance imaging (MRI) today occupies an important place among imaging methods due to its high contrast of soft tissues, the absence of ionizing radiation and flexibility in choosing signal weighting modes. Due to these properties, MRI is widely used in neuroimaging, orthopedics, oncology and cardiology [1,2]. In global clinical practice, magnetic resonance imaging machines with a field induction of 1.5 T remain the most common and affordable. They are used as the main imaging standard due to the optimal ratio of image quality, examination time and economic feasibility. Despite the lower signal-to-noise ratio compared to 3T systems, it is 1.5 T devices that are used in the vast majority of clinical cases, including oncological, cardiological and neurological studies. However, despite its high informative value, MRI remains very sensitive to noise and artifacts. These can arise both from hardware limitations (scanner characteristics, multichannel coils, excitation and reconstruction parameters) and from physiological factors, including involuntary patient movements, breathing, or magnetic field inhomogeneities [3,4]. Such factors directly affect the signal-to-noise ratio (SNR) and, in the case of insufficient image quality, can make diagnosis difficult or even impossible. This makes it relevant to conduct research on methods for increasing information content and reducing the impact of noise specifically for 1.5 T MRI, since the results obtained will have the greatest practical value and wide application.

To reduce these negative effects, denoising methods are being actively developed. Classical algorithms are based mainly on synthetic noise models, primarily Gaussian or Rician [5,6]. Their popularity is due to their mathematical simplicity and the possibility of rapid implementation. At the same time, they do not reflect the complex statistical nature of real noise in MRI. For example, Rician noise has been shown to be SNR-dependent and has properties that significantly change the intensity distribution, especially in low-signal areas [7]. Ignoring these effects results in methods that work well on artificially noisy images showing lower performance in clinical settings. The current trend in MRI denoising is to use methods that can reproduce the characteristics of real noise and take into account the physics of signal formation. Considerable attention is paid to deep learning, which has radically changed the approach to medical image processing in the last decade [8,9]. In particular, self-supervised and unsupervised methods are actively developing, which allow training models without ideal "reference" data, which is often unavailable in medicine [10,11]. Another direction is to model noise directly in k-space, i.e. in the original data before reconstruction. This allows you to create artifacts that are as close to real ones as possible and thus form more reliable training samples [12].

A special place is occupied by research using physical phantoms [13]. Although the study was conducted in the context of radiography, it clearly demonstrates the general methodological approach and the importance of phantom

Cite as: D.G. Sliusarenko, A.V. Netreba, East Eur. J. Phys. 1, 413 (2026), https://doi.org/10.26565/2312-4334-2026-1-50

studies for clinical verification of image processing algorithms. They provide controlled experimental conditions, allow for statistical description of noise distribution, and test algorithms in repeatable scenarios [14]. Recent work demonstrates that combining phantom data and k-space noise modeling can increase SNR, reduce artifacts, and bring reconstruction results closer to clinically relevant ones [15,16]. This confirms the importance of moving from purely synthetic models to more realistic ones based on physical experiments. At the same time, with the development of modeling methods, the architectures of neural networks used in medical imaging are also being actively improved. The use of attention mechanisms such as CBAM (Convolutional Block Attention Module) or channel-wise attention [9], as well as integrating multilevel noise statistics into the model [15], allow to increase the accuracy of reconstruction of small structures and better preserve diagnostically important information. This approach opens up the prospect of creating more universal denoising systems capable of working on both phantom and clinical data. The aim of this study is to develop a method for denoising MRI images that combines statistically sound modeling of signal degradations based on phantom experiments with an improved neural network architecture that integrates attention mechanisms and takes into account noise characteristics at deep levels of the model. The proposed approach is aimed at improving the clarity of reconstructed images and preserving diagnostically significant information when working with standard clinical data.

2. Materials and methods

2.1. Phantoms and their characteristics

The study used specially prepared phantoms designed to simulate different types of biological tissues and analyze the impact of noise on the quality of magnetic resonance images. The use of phantoms provides controlled experimental conditions, which allows for a systematic study of noise characteristics in a reproduced environment and comparison of the results with literature data [17,18]. We used three types of Siemens phantoms (Table 1), which allow for the simulation of different tissue-like environments and the analysis of the effect of noise on magnetic resonance images. The first of them is a cylindrical phantom with a volume of 5300 ml, filled with a solution containing 3.75g $NiSO_4 \cdot 6H_2O$ and 5 g NaCl per 1000 g of distilled water. This combination reproduces the electrical conductivity of soft tissues and allows you to control the electromagnetic properties during measurements. The second object was a spherical phantom D165 with a diameter of 165mm and a volume of 2570ml, in which a solution of 1.25 g of $NiSO_4 \cdot 6H_2O$ per 1000 g distilled water. Due to its high homogeneity and stability, this phantom was intended to reproduce conditions with controlled SNR, which provides an assessment of the basic noise characteristics and parameter calibration. The third phantom was a spherical D240 with a diameter of 240 mm and a volume of 7300 ml, filled with Marcol oil with the addition of 0.011g of Macrolex blue dye per 1000ml. It was used to simulate adipose tissue and model inhomogeneities, which allows assessing the appearance of artifacts and the robustness of denoising algorithms to differences in tissue structure. Phantom data were acquired on a 3-Tesla MR scanner (Siemens MAGNETOM Vida). The dataset included two different 3D T1-weighted sequences with high isotropic resolution (1x1x1 mm). The first sequence was a 3D gradient echo (MPRAGE/TFL) with inversion-recovery (TR=2300 ms, TE=2.96 ms, TI=900 ms, 9° Flip angle). The second was a 3D fast spin echo (SPACE) (TR=700 ms, TE=22 ms, 120° Flip angle).

Table 1. Names and characteristics of phantoms used for analyzing the statistical characteristics of superimposed noise.

PHANTOM	SIZE / VOLUME	SOLUTION COMPOSITION	PURPOSE
Cylindrical (5300 ml)	Height = standard; Volume: 5300 ml	3.75 g $NiSO_4 \cdot 6H_2O$ + 5 g NaCl per 1000 g dist. H_2O	Simulation of homogeneous soft tissues, conductivity regulation
Spherical D165	Diameter: 165 mm; Volume: 2570 ml	1.25 g $NiSO_4 \cdot 6H_2O$ per 1000 g dist. H_2O	Assessment of homogeneity and basic noise characteristics, SNR calibration
Spherical D240	Diameter: 240 mm; Volume: 7300 ml	Marcol oil + 0.011 g Macrollex Blue per 1000 ml	Simulation of adipose tissue and inhomogeneities, artifact analysis and algorithm robustness

Phantoms are widely used in medical imaging for quality control, standardization of experiments, and improvement of algorithms [17], and can also serve as a proxy metric for scan quality to increase research reproducibility [19].

2.2. Frequency domain noise modeling

In magnetic resonance imaging, the signal is formed in the frequency domain (k-space) as complex samples. The image is reconstructed in coordinate space by means of the inverse Fourier transform [20]:

$$I(x,y) = \mathcal{F}^{-1}K\big(k_x, k_y\big), \tag{1}$$

where $K(k_x, k_y)$ - complex k-space data, and $I(x,y)$ - reconstructed MRI image.

This study uses standard clinical DICOM images, which retain only the magnitude of the reconstructed signal and do not contain phase information or the original complex-valued k-space data. Therefore, any k-space obtained by inverse Fourier transform of magnitude images is a pseudo-k-space, which is not a physical representation of the frequency data

acquired by the scanner. In this regard, this work does not claim to directly denoise true k-space, but uses the frequency representation solely as a mathematical tool for modeling and analyzing image degradation. It is known that noise in raw MRI data arises as additive complex Gaussian noise in k-space, due to thermal fluctuations of the receiving system (effective resistance of the receiving coil and the specimen) [21]. Since the original complex data is not available, this noise cannot be accurately reproduced or removed in a physically rigorous sense. In this paper, complex Gaussian noise is considered as a reference physical model that explains the origin of non-Gaussian effects in image space, but is not used to directly model the true k-space of the scanner. After reconstruction and calculation of the magnitude of the complex signal:

$$M(x,y) = \sqrt{I_r^2(x,y) + I_i^2(x,y)}, \tag{2}$$

in the presence of complex Gaussian noise, a ray-like distribution of intensities naturally arises, especially in regions with a low signal-to-noise ratio [22]. In this work, these effects are not artificially introduced, but are considered as a consequence of the standard reconstruction process. In addition to noise, real MRI images may contain degradations associated with patient motion, reconstruction instability, or further processing. Such effects are not interpreted as physical k-space noise and are applied only at the image level as part of a training strategy to increase the robustness of the neural network. Therefore, the presented approach is not a direct denoising of physical k-space, but is aimed at improving the quality of reconstructed MRI images obtained from standard DICOM data. The frequency representation is used as a convenient mathematical tool, while all assumptions about the nature of MRI noise are consistent with the limitations of the available data.

2.3. Statistical analysis of noise

To quantify the impact of different types of noise on MRI phantom images, three key statistical characteristics were measured: mean, skewness, and kurtosis, as a function of noise intensity. The use of histogram parameters such as skewness and kurtosis is a validated approach for analyzing image heterogeneity and shape distribution [23]. In particular, the mathematical representation of excess kurtosis and statistical significance through sample moments allows us to clearly quantify how much noise deviates from a normal distribution [24]. To quantitatively characterize the impact of scanning artifacts on the quality of MR images, a series of experiments using phantoms was conducted. One group of phantoms was scanned under optimal conditions (“clean” phantoms), the other group was scanned under conditions of light artifacts: metal (iron) impurities, accelerated gradient echo (GRE) sequences, minimal noise amplification, or magnetic field instability. Figure 1 shows an example of a pair of clean and noisy images in the case of noise damage to a metal artifact The statistical values are given for this specific pair of images.

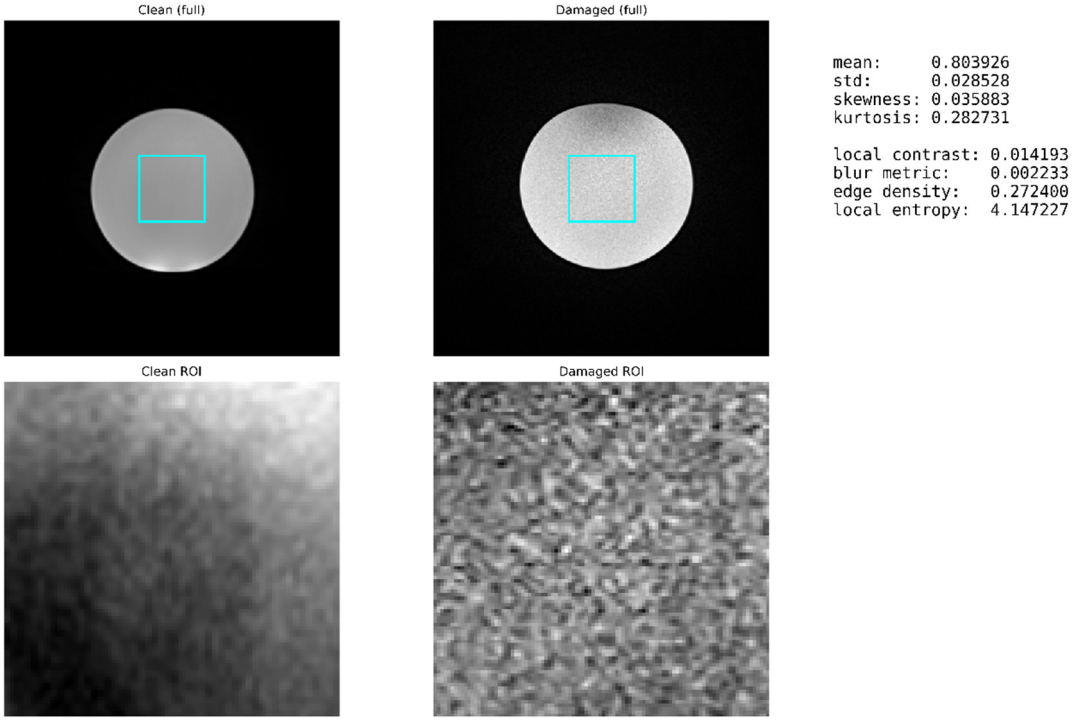

Figure 1. Examples of phantom images and obtaining statistical characteristics.

In each case, the following statistical indicators of pixel intensities were calculated within the specified ROIs (regions of interest):

$$\text{mean} = 0.77, \text{std} = 0.033, \text{skewness} = 0.27, \text{kurtosis} = 0.51.$$

The mean intensity value reflects the generalized signal level in the ROI and allows for the assessment of possible baseline level bias caused by scanning artifacts. Standard deviation (σ) characterizes the variability of intensities, i.e. internal signal fluctuations and noise-like effects caused by magnetic field inhomogeneity or metallic inclusions. Distribution asymmetry (skewness, γ_1) determines the degree of shift of the intensity histogram: a positive value (0.27) indicates a predominance of pixels with higher intensity, reflecting local amplifications or slight signal saturation. Kurtosis (kurtosis, γ_2) describes the peakedness of the distribution - a value of 0.51 indicates a moderate concentration of intensities around the mean and the presence of slight "tails" due to scanning artifacts.

The obtained values demonstrate that even without intentionally synthesized noise, real scanning conditions (artifacts) change the signal statistics - increase the dispersion (std), create asymmetry (positive skewness) and slight "sharpness" (kurtosis). Such behavior confirms the feasibility of using these statistical indicators as input features for the StatsProjection module in the network, allowing to adapt the filtering depending on the nature of the artifacts. Phantoms were scanned three times in each mode; the resulting images were pre-normalized to [0,1] and scaled to 512*512 pixels. ROIs were placed in the central region of the phantom (homogeneous zone), excluding borders and large artifacts. Mean, std, skewness, and kurtosis were calculated for each series and then averaged. The resulting values are shown above. This statistical evaluation confirms the presence of stable artifact-induced signal fluctuations that are not labeled as pure noise but affect image quality at the histogram level. Therefore, integrating these statistics into network training allows for better adaptation of the model to real scanning conditions and increases its generalizability.

These values were integrated into the preprocessing block, which generates noise patterns with statistical properties as close as possible to real ones. This approach allows the model to take into account not only the average noise level, but also its asymmetry and the shape of the distribution, which is important for reproducing realistic noise artifacts during training.

2.4. Improved neural network architecture

The proposed model is designed to denoise MRI images of size 512*512 pixels (1 channel, grayscale) taking into account the physical characteristics of the noise measured on phantoms and statistical parameters integrated into the training process. The architecture combines the advantages of U-Net [25] with residual connections, attention mechanisms, multiscale processing (ASPP) [26] and statistical integration module (StatsProjection) [27]. This combination allows for effective noise suppression while preserving contours, texture, and diagnostically significant image details. Residual blocks with SpatialDropout (Regularization Method for CNNs) [28] and LeakyReLU (Leaky Rectified Linear Unit) [29] are used to avoid information loss during convolutions due to residual connections, improve the generalization ability of the model through spatial dropout, and prevent the disappearance of the gradient by using LeakyReLU activation.

The model implements a residual approach to denoising: it does not directly reconstruct a clean image, but learns to reproduce the noise map $R_\theta(I_{noisy})$ after which the reconstructed image is defined as:

$$\hat{I} = I_{noisy} - R_\theta\big(I_{noisy}\big), \tag{3}$$

where I_{noisy} - noisy input image, $R_\theta(\cdot)$ - function approximating the noise structure, $\hat{I}$- de-noised image. The real (reference) image is marked as I_{gt} and is used as a reference when calculating the loss function. This approach accelerates convergence and stabilizes learning, since the network operates with less dynamic values (the amplitude of the noise is smaller than that of the signal). The architecture is based on U-Net with a symmetric encoder and decoder connected by skip connections. Each level consists of the following elements:

Residual blocks (ResBlock):

$$y = F(x, W_i) + x, \tag{4}$$

where $F(x, W_i)$ - sequence of convolution, normalization and activation operations of LeakyReLU.

Adding input signal x prevents information loss in deep convolutions and reduces the risk of gradient vanishing. Using SpatialDropout2D preserves spatial consistency by suppressing random overcorrelations between filters. CBAM is essentially an attention mechanism operating in two dimensions [30]:

- Channel Attention amplifies the most informative channels:

$$M_c = \sigma\left(W_2\left(\delta\left(W_1\big(GAP(x)\big)\right) + W_1\big(GMP(x)\big)\right)\right), \tag{5}$$

where GAPi GMP - global averaging and maximum operations, σ - sigmoid, δ - ReLU.

- Spatial Attention focuses on local areas of the image:

$$M_s = \sigma\big(f^{7\times7}([AvgPool(x); MaxPool(x)])\big). \tag{6}$$

Final gain:

$$x' = M_s \odot (M_c \odot x). \tag{7}$$

ASPP is used in the "neck" of the network for multi-scale analysis, providing sensitivity to different spatial frequencies of noise. It uses convolutions with extensions d = [1,6,12,18], after which the results are combined:

$$y_{ASPP} = \sum_i Conv_{3\times3}^{(d_i)}(x). \tag{8}$$

Channelwise Attention (CA) takes into account the global interaction between channels by calculating weights via a normalized softmax vector [31]:

$$w_i = \frac{e^{g_i}}{\sum_j e^{g_j}}, \text{where } g_i = \text{GAP}(x_i). \tag{9}$$

This improves the balance between high-frequency and low-frequency features, especially in areas with heterogeneous SNR.

The StatsProjection module implements the idea of physically based feature adaptation, where parameters obtained from statistical noise analysis directly influence the process of normalizing activations in a neural network [32]. Unlike standard normalization mechanisms which calculate scaling and shifting parameters directly from the data in the current layer, this module uses external experimentally measured noise characteristics - the average μ, standard deviation σ, asymmetry skewness and kurtosis obtained from phantom studies. The input to the module is a four-dimensional vector of statistical parameters:

$$s = [\mu, \sigma, \text{skewness}, \text{kurtosis}],$$

which describes the statistical “profile” of noise for a particular image or its fragment. This vector is fed to a fully connected layer (Dense) with linear activation, which performs the projection of statistical parameters into the feature scale space:

$$v_s = W_s \cdot s + b_s, \tag{10}$$

where W_s and b_s - parameters of the training layer. The resulting vector v_s has the same number of components as the number of channels in the current feature tensor x, and therefore can be used to modulate normalization. After this, the normalized activations are corrected, where the vector v_s acts as a scaling modifier:

$$y = \text{Norm}(x) \odot (1 + v_s), \tag{11}$$

where $\text{Norm}(\cdot)$ - Layer Normalization, which provides zero mean and unit variance within the layer, $\odot$ - per-channel multiplication. Thus, StatsProjection adds a physically meaningful scaling to the standard normalization process, which aligns the network with the real noise statistics inherent in a particular data type.

Intuitively, this approach resembles the Feature-wise Linear Modulation (FiLM) method, but with the difference that the modulating parameters are not trained directly from the data, but are derived from experimentally measured noise statistics. This provides better consistency of the network with the physical characteristics of the MRI signal, allows it to respond adaptively to different types of artifacts, and stabilizes training when working with heterogeneous data sets.

The loss function combines several components:

$$\mathcal{L}_{total} = \lambda_1 \mathcal{L}_{MSE} + \lambda_2 \left(1 - SSIM\left(\hat{I}, I_{gt}\right)\right) + \lambda_3 \mathcal{L}_{GDL}, \tag{12}$$

where:

$\mathcal{L}_{MSE}$ - minimizes the energy difference between $\hat{I}$ and I_{gt};

$SSIM$ - structural similarity controlling local contours;

$\mathcal{L}_{GDL}$ - gradient loss that prevents blurring of boundaries;

λ_i - weighting factors (0.5, 0.3, 0.2 respectively).

During training, the model receives a pair(I_{noisy}, I_{gt}), where I_{noisy} - images with physically motivated degradations obtained by frequency perturbations of reconstructed magnitude images, and I_{gt} - phantom or clinical image with high signal-to-noise ratio. Thus, the network is trained on degradations consistent with the physical properties of MRI, rather than on arbitrary synthetic noise [33-35].

All convolutional layers of the model use 3*3 kernels with “same” padding and HeNormal weight initialization. [36], which ensures stable variation of activations even in deep layers. The use of residual connections between the encoder and decoder allows to transfer not only contextual, but also textural information, which is critically important for MRI images, where soft tissue contrast often has a fine gradation. The combination of CBAM, ASPP and Residual-blocks

creates a balance between global contextuality and local detail, ensuring the preservation of anatomical structures with effective noise suppression. The final view of the model is presented in Figure 2.

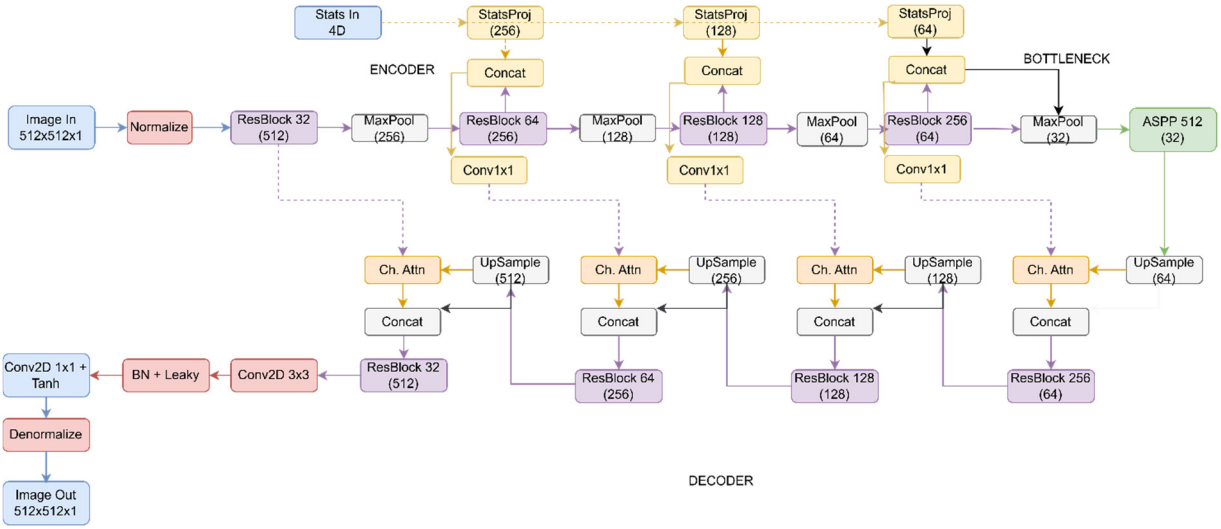

Figure 2. Structural diagram of the model used for processing, reconstruction and denoising of noisy images

2.6. Model training

To ensure the reliability and reproducibility of the training results, the model was trained on structured subsets of MRI images formed according to the principles of sample independence. The main data set consisted of normalized 16-bit MRI images of 512x512 pixels in grayscale. Each subset contained unique samples, which excluded any overlap between the data for training, validation, and testing. To control the generalization ability of the model, training was carried out on the training sample (60%) with periodic checking on the validation subset (20%). The final efficiency was assessed on an independent test set (20%), which was not used at any stage of training. Thus, the obtained results characterize the real ability of the model to generalize data that were not encountered during parameter optimization. Overtraining control was provided by mechanisms that automatically adjusted the learning rate and fixed the best model weights with minimal validation error. During the simulation, various types of physically based noise were implemented: Rician, Gaussian, Poisson and salt-and-pepper, each of which was generated with random intensity parameters according to the amplitude characteristics of the output signal in k-space. After the inverse Fourier transform, images with specified statistical properties of the noise were obtained, which formed training pairs. Both types of input data were used in the training process: noisy images and vectors of statistical noise parameters (mean, standard deviation, skewness, kurtosis), which were fed into the StatsProjection Module for adaptive modification of normalization. Training was performed using the AdamW optimizer (learning rate $= 1 \times 10^{-4}$, $\beta_1 = 0.9$, $\beta_2 = 0.999$) and dynamic adjustment of the learning rate according to the scheme. Mixed-precision training and Batch Renormalization in deep layers were used to stabilize convergence.

The criterion for completing training was the achievement of stabilization (plateau) of the validation error, i.e. the moment when subsequent epochs did not lead to an improvement in the results on the validation data. For this, an early stopping mechanism was used, which automatically stops optimization after 10 epochs without improving the quality of the model and restores the weights fixed at the best stage. Additionally, an adaptive learning rate adjustment algorithm was used, which reduces it by 5 times (factor 0.2) after 5 epochs without improving the results, but not below the minimum value 1×10^{-6}. This combination of methods prevents overfitting, stabilizes convergence, and allows the model to gradually approach the global minimum of the loss function without losing generalization ability. Training was performed with a batch size of 16, for 50-100 epochs, depending on the experiment, on an NVIDIA RTX 5070 Ti graphics accelerator.

2.7. Methods for quantifying image quality

To quantify the effectiveness of the proposed denoising model, both reference and non-reference metrics were used, which allow us to assess the quality of signal recovery, preservation of structural similarity, local contrasts, and signal homogeneity within regions of interest. This approach allows us to comprehensively characterize both the intensities and structural reliability of the results obtained, combining analytical accuracy with clinical relevance.

The Peak Signal-to-Noise Ratio (PSNR) metric is defined as [37]:

$$PSNR = 10 \cdot \log_{10}\left(\frac{MAX_I^2}{MSE}\right), MSE = \frac{1}{N}\sum_{i=1}^{N}(I_i - \hat{I}_i)^2, \quad (13)$$

where MAX_I - maximum intensity value, I_i and $\hat{I}_i$- pixel values in the reference and reconstructed images, respectively. PSNR is a classical metric for assessing the degree of signal distortion and is based on the energy distance between the

input and reconstructed images. High PSNR values indicate minimal signal loss, but this metric does not take into account the perceptual aspects of the image [38].

To eliminate this drawback, the Structural Similarity Index is used [37,39], which describes the structural similarity between two images, taking into account brightness, contrast, and texture:

$$SSIM(I,\hat{I}) = \frac{(2\mu_I\mu_{\hat{I}}+C_1)(2\sigma_{I\hat{I}}+C_2)}{(\mu_I^2+\mu_{\hat{I}}^2+C_1)(\sigma_I^2+\sigma_{\hat{I}}^2+C_2)}. \quad (14)$$

Here μ_Ii $\mu_{\hat{I}}$ - average intensity values, σ_I and $\sigma_{\hat{I}}$- dispersion, $\sigma_{I\hat{I}}$- covariance between images. SSIM evaluates not only numerical similarity, but also the degree of preservation of textural and spatial relationships, which makes it more consistent with human perception of quality. Since for medical images it is important not only to preserve the average signal level, but also to avoid loss of contours, the Edge Preservation Index (EPI) is used:

$$EPI = \frac{\sum|\nabla\hat{I}|\cdot|\nabla I|}{\sum|\nabla I|^2}. \quad (15)$$

This indicator is based on comparing image gradients and reflects the degree of edge preservation after denoising [40,41]. A high EPI value indicates that the model does not blur the structure and adequately restores local intensity transitions, which is critical for diagnosing gray-white matter boundaries or tumor contours. Another fully reference metric is the Normalized Cross-Correlation (NCC) [42]:

$$NCC = \frac{\sum(I-\mu_I)(\hat{I}-\mu_{\hat{I}})}{\sqrt{\sum(I-\mu_I)^2\sum(\hat{I}-\mu_{\hat{I}})^2}}. \quad (16)$$

It determines the degree of linear relationship between two images regardless of scale variations. NCC is particularly useful for assessing the stability of reconstructions, where it is important to maintain spatial correlation even if the absolute values of the intensities change. For real clinical MRI images, where there is no “gold standard”, non-reference indicators Signal-to-Noise Ratio were additionally used [43] and Coefficient of Variation (CV) [44,45], which are calculated within ROIs (regions of interest). They have the form:

$$SNR = \frac{\mu_{signal}}{\sigma_{noise}}, CV = \frac{\sigma_{ROI}}{\mu_{ROI}}. \quad (17)$$

Here μ_{signal} and σ_{noise}- mean and standard deviation of signal and noise, respectively, while CV characterizes the relative intensity heterogeneity within the selected region. An increase in SNR after denoising reflects a real improvement in tissue contrast, and a decrease in CV indicates a decrease in local fluctuations and stabilization of signal homogeneity. Such indicators are closer to the clinical perception of quality, since they characterize not only the technical accuracy of the reconstruction, but also the diagnostic readability of the image. In general, the combination of reference (PSNR, SSIM, EPI, NCC) and non-reference (SNR, CV) metrics provides a comprehensive assessment of image quality, covering both structural reliability and practical suitability for clinical analysis [36,46,47]. This approach is consistent with current recommendations for medical imaging tasks, where there is no single standard for a true image, and quality assessment should take into account both physical and perceptual aspects.

2.8. DICOM medical images used

To train and test the model, 5000 anonymized DICOM (Digital Imaging and Communication in Medicine) brain MRI images obtained from 200 patients were used. All images were previously anonymized, which guaranteed patient confidentiality. The dataset consisted of T1-weighted images, which are necessary for clear visualization of the anatomical structure of the brain and differentiation of gray and white matter. A heterogeneous set of T1-weighted brain MRI images obtained on 1.5 T scanners from different manufacturers (Siemens Symphony and GE Optima MR450w) was used for the study. The 2D sequences included conventional spin echo (SE) from Siemens (TR/TE 394/17 ms; slice thickness 5 mm) and fast spin echo (FSE) from GE (TR/TE 623/7.776 ms; slice thickness 5 mm). To simulate real-world scenarios of image degradation, noise of various ranges and characteristics was artificially added to the original data. In addition, artifacts associated with k-space truncation (Gibbs bell) and motion were simulated. This variety of noise allowed the model to be trained to work effectively in conditions as close as possible to clinical practice, where the quality of the original data can vary significantly. Particular attention was paid to the uniformity of brightness and contrast between image series, as these parameters affect the stability and accuracy of the algorithms. To this end, subsets of images with high SNR levels were generated, which were used as reference examples (ground truth) to evaluate the effectiveness of noise reduction. A separate and comprehensive validation set was also created to ensure an adequate reflection of the variety of clinical cases that the model may encounter in practical application.

3. Results and discussion

3.1. Quantitative assessment

Three key metrics were used to evaluate the effectiveness of the proposed denoising method: PSNR, SSIM, and EPI. PSNR and SSIM metrics are widely used in modern MRI denoising work, including studies of score-based self-learning

MRI denoising, systematic analysis of wavelet-based approaches for brain MRI images, and recent work on self-learning diffusion MRI denoising [4]. Their effectiveness is also confirmed in a comprehensive review of medical image quality assessment systems, which highlights the critical importance of accurate metrics for diagnosis and clinical outcomes [48]. EPI allows for the addition of an important dimension of local edge and contour preservation -critical for medical diagnostics-and has already been proven to be an objective and reliable metric in MR image restoration tasks compared to subjective assessment [49]. Additionally, the use of PSNR, MSE, and SSIM as "image quality metrics" when comparing denoising algorithms is supported by studies of quality assessment of full-reference methods for medical images, which demonstrate a correlation between objective metrics and subjective quality [50,51]. Overall, the results for all three metrics confirm that the use of statistically sound noise parameters in k-space allows for a significant improvement in image quality (Fig. 3).

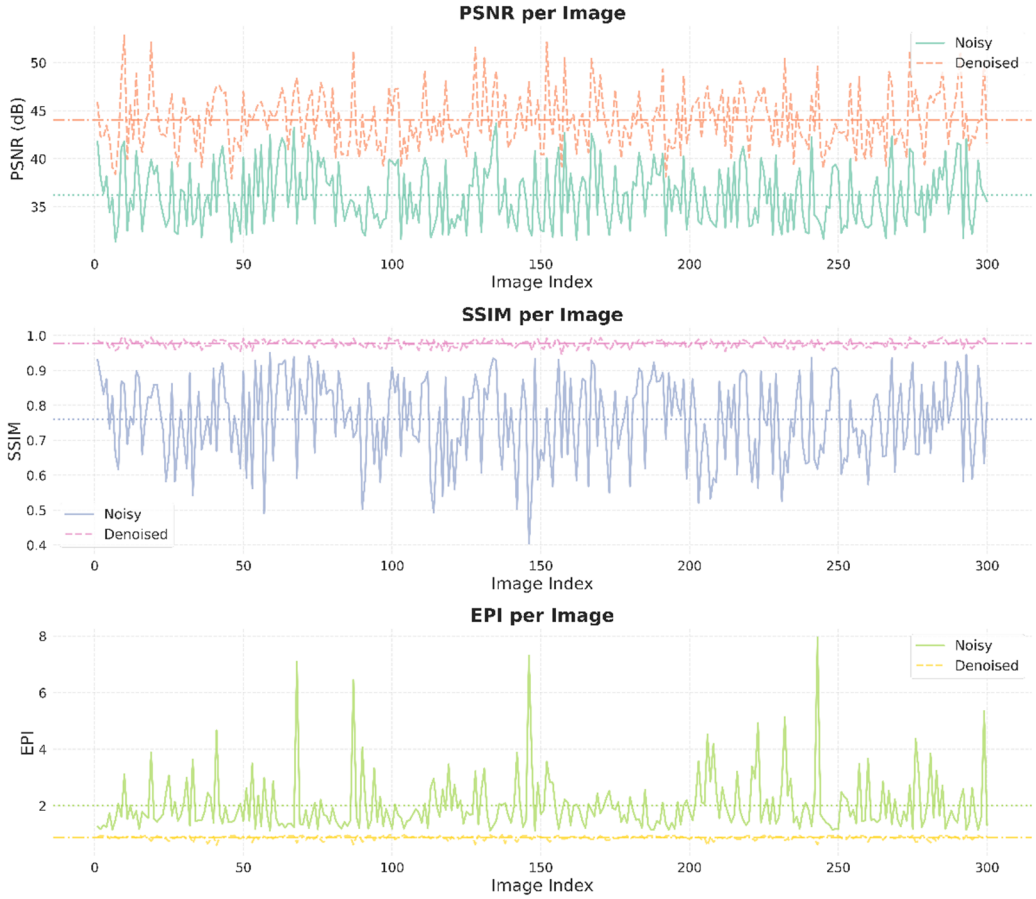

Figure 3. Graphs of the obtained PSNR, SSIM and EPI results for 300 real images after adding noise of different intensity gradations to simulate real scanning conditions.

PSNR is a basic numerical criterion of reconstruction quality, reflecting the ratio between the maximum possible signal intensity and the root mean square error. It is important to note that the calculation was performed based on the dynamic range of 16-bit DICOM data, which results in higher absolute values compared to standard 8-bit formats. In the presented experiments, noisy images had PSNR values in the range of 28-41 dB, which indicates signal degradation. In contrast, after denoising, improvement of up to 40-54 dB was observed. It is important to note the stable difference of approximately 8-10 dB between the processed and unprocessed images, which indicates the consistency of the algorithm regardless of variations in the source data.

Since PSNR does not take into account perceptual aspects, for a more adequate assessment, the SSIM metric, which reflects the similarity of structural characteristics between the original and the reconstructed image, was also used. For noisy data, the SSIM varied in a wide range of 0.5-0.95, demonstrating instability and loss of structural information. After applying the denoising algorithm, the SSIM values stabilized at 0.95-1.0, which confirms the ability of the model to preserve small structural elements and image topology even at different noise levels. Special attention was paid to the EPI metric, which assesses the quality of contour and fine detail restoration. In noisy images, EPI ranged from 1.0 to 8.0, with sporadic peaks reflecting local artifacts caused by noise. After denoising, EPI values stabilized around 1.0, indicating a high level of edge preservation and no additional blurring or structural loss during processing.

The proposed approach provides not only an increase in the signal-to-noise ratio, but also the restoration of structural similarity and the correct preservation of fine details, which is critically important for clinical diagnostics. Additionally, histograms of the distribution of metric improvements were constructed for all images for quantitative analysis. The

distribution graph for PSNR improvements shows a clear shift to the right with an average increase of 7.85 dB, which confirms a stable noise reduction in most images. A similar trend is observed for SNR improvements, where the average increase is also 7.85 dB, indicating an increase in the signal-to-noise ratio and improved visibility of structural details. For SSIM improvements, the average increase is 0.217, which reflects improvement in the structural similarity of denoised images to the original "clean" data. This is particularly important because SSIM better accounts for human perception of local details and textures than PSNR. In the case of NCC improvements, a more compressed distribution is observed with an average gain of 0.046. Although this value is small compared to other metrics, even a small improvement in NCC indicates a higher stability of the correlation between the denoised and reference images. Thus, all four histograms demonstrate that the improvement is systematic and covers most of the data, rather than being limited to isolated cases (Fig. 4). This confirms the consistency of the model's performance across samples and highlights its suitability for practical use.

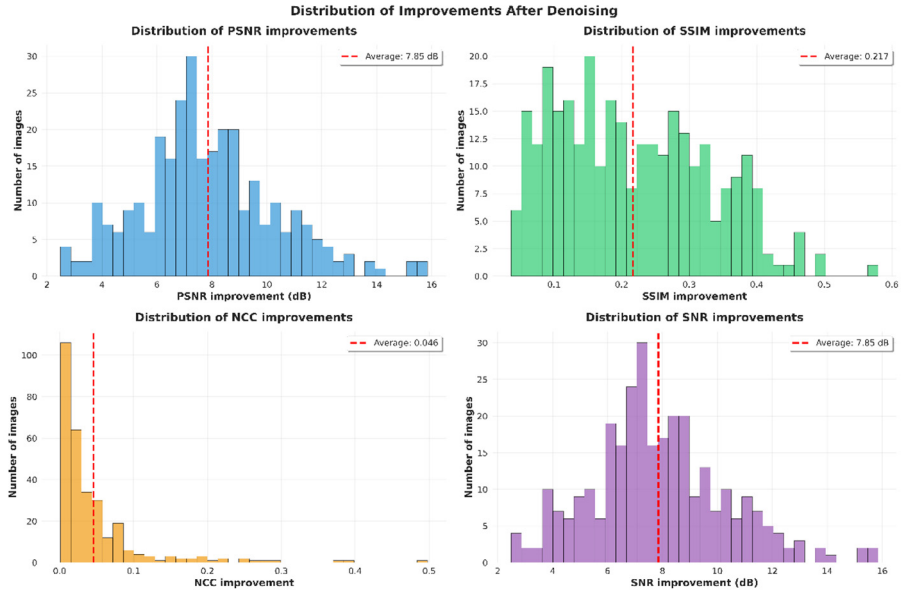

Figure 4. Histograms of the distribution of improvements in the PSNR, SSIM, NCC, SNR metrics for all images.

Visual evaluation also shows that our method provides good perceptual quality (Fig. 5).

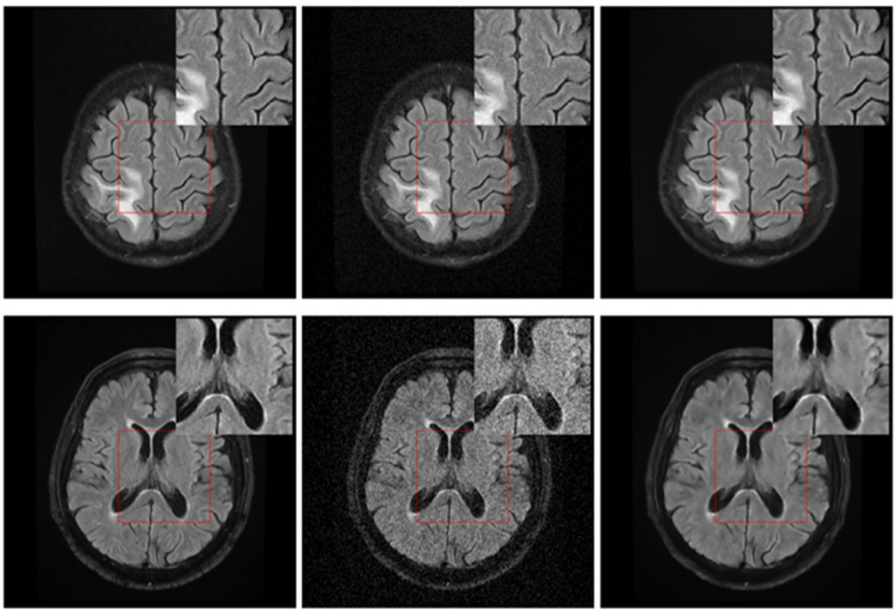

Figure 5. Subjective comparison of several DICOM T1 images before adding strong artificial noise (left), with noise (center) and after processing with the developed model (right)

Our method consistently preserves fine anatomical details, especially in areas of complex tissue boundaries, without characteristic smoothing artifacts. In white matter regions, our method demonstrates exceptional preservation of subtle intensity variations critical for detecting pathological changes. The gray matter-cerebrospinal fluid interface is one of the most challenging areas to denoise due to abrupt intensity transitions. Our method excellently preserves sharp boundaries,

avoiding the characteristic discretization artifacts of deep networks. CNN (Convolutional Neural Network) methods introduce subtle geometric distortions near these boundaries, which can affect morphometric analysis. For T1 images, where hyperintensities are clinically relevant, our method demonstrates optimal preservation of pathological lesion contrast while effectively suppressing background noise. For visual evaluation, randomly selected images are presented, to which strong noise was added, simulating difficult acquisition conditions, to demonstrate the effectiveness of the proposed model even in cases of significant deterioration in the quality of the original data.

To test the generalization ability of the model and its practical applicability, an evaluation of its effectiveness was carried out on real clinical MRI images of the brain obtained on a Siemens MAGNETOM Aera tomograph (1.5T). Unlike the test set with artificially simulated noise, these images did not have standards, so the analysis was carried out using ROI-based metrics that do not require a "clean" reference sample. For each image, regions of interest were automatically formed: the central zone of homogeneous signal, the peripheral background area and the edge area between contrasting tissues. Based on these areas, the main quantitative characteristics were calculated - SNR, coefficient of variation and edge sharpness, which reflect the physical quality of the reconstructed signal. The general principle of obtaining the difference between the noise in the original and denoised image is shown in the Figure 6.

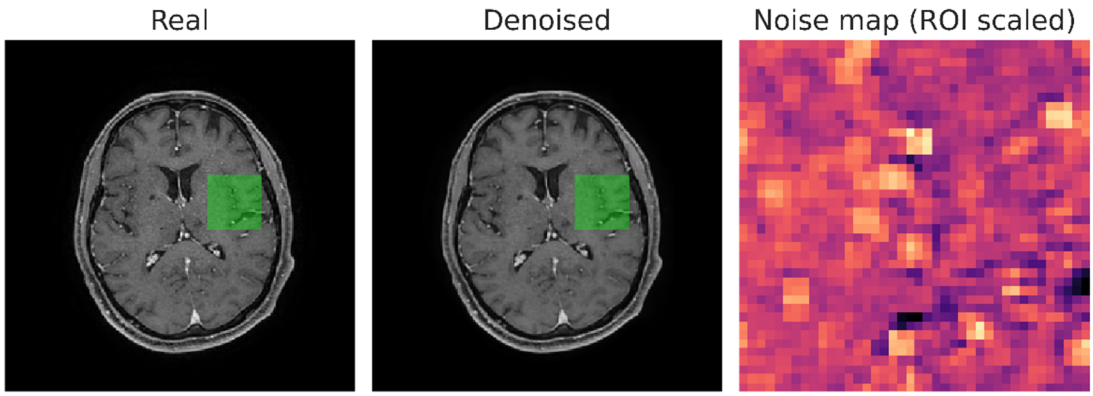

Figure 6. One slice from the evaluation set of clinical MRI T1 images and the noise map of the difference between images

200 images from different series of T1-weighted scans were selected for the study. The results showed a increase in the signal-to-noise ratio after applying the model, indicating a reduction in noise while maintaining contrast between tissues. Quantification of 200 clinical T1 slices demonstrated consistent but modest improvements in ROI-based SNR (+6-8%) and reductions in coefficient of variation (-4-7%) (Fig. 7). Importantly, the model preserves anatomical detail, as reflected by the nearly overlapping profiles of the "before" and "after" curves. Thus, the reconstructed images are characterized by higher stability of intensities with minimal loss of spatial details.

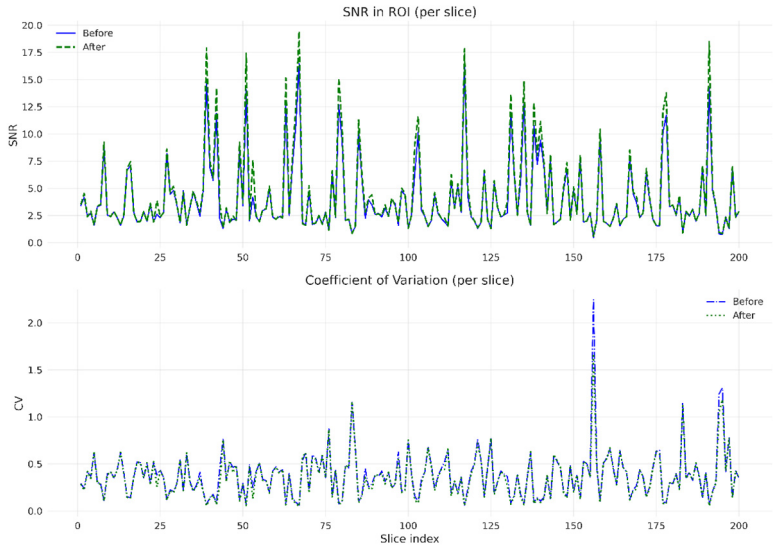

Figure 7. SNR and CV graph of 200 selected real clinical images of brain T1 images

Visual analysis confirms the obtained numerical results. After processing, there is a reduction in high-frequency fluctuations and inhomogeneities, preservation of fine structures of the cerebral cortex, white matter and contours of intertissue boundaries. Signals in homogeneous areas become more uniform, and intensity histograms demonstrate a narrowing of the distribution around the mean, which is a characteristic sign of noise reduction without loss of contrast.

To evaluate the quality of real clinical image processing in specific areas of interest, the Axial T1-weighted FSE (Fast Spin Echo) sequence was chosen. This scan is a standard 2D high-resolution anatomical sequence that is widely used in routine diagnostics. It provides excellent soft tissue contrast and clear anatomical detail due to optimized spin-lattice relaxation time. Based on a gradient echo complex, FSE is less sensitive to magnetic field inhomogeneities, making it a reliable reference for evaluating the effectiveness of noise suppression in realistic clinical scenarios. The results are shown in Figure 8.

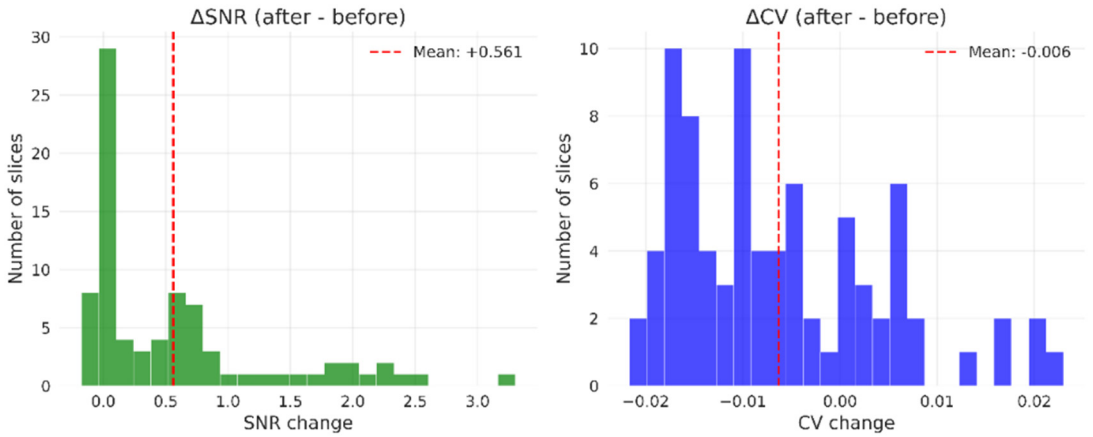

Figure 8. Histogram of the distribution of SNR and CV values of Axial T1-weighted Fast Spin Echo sequences after processing by the model

The results obtained show that the model trained on phantom and synthetically noisy data successfully generalizes its knowledge to real clinical images. We obtained an increase in the signal-to-noise ratio by an average of 11% and a decrease in noise by 3%. Since the selected scans already have quite good image quality in the original case, this confirms the correctness of the integration of phantom noise statistics through the StatsProjection module, which provides a physically justified adaptation of feature normalization to a specific noise level. As a result, the model not only improves the visual perception of MRI images, but also increases the metric reliability of the signal, which is of direct importance for clinical applications, in particular for the accurate alignment of MRI and CT during radiotherapy planning. Thus, the evaluation on real data confirms the effectiveness and robustness of the proposed method, which can be integrated into standard clinical protocols as a stage of pre-processing of medical images.

3.2. Comparison with existing methods

The performance of the proposed neural network-based denoising approach considering k-space noise statistics was evaluated against established denoising methodologies to demonstrate its advantages in improving the quality of MRI images (Table 2). Quantitative analysis revealed significant improvements in all evaluated metrics compared to traditional and state-of-the-art methods.

Recent advances in deep learning have revolutionized MRI denoising, and several notable architectures have achieved impressive results. The DnCNN (Denoising Convolutional Neural Network) architecture [52] – one of the pioneering deep learning approaches for image denoising -typically achieving PSNR improvements from 36–38 dB to 42–44 dB in MRI applications. However, these methods typically operate in the spatial domain of the image and do not model the data acquisition process in k-space.

RED-CNN approach (Residual Encoder–Decoder Convolutional Neural Network) [53] specifically designed for medical imaging, demonstrates comparable performance with PSNR values of 39–45 dB, but lacks the physical justification characteristic of our approach.

Unsupervised learning methods such as Noise2Noise (Learning to Denoise from Corrupted Images) and Noise2Void (Learning Denoising without Clean Data) have attracted attention due to their ability to work without paired sets of "clean" images. According to a review by Wang et al. (2020) [54], Noise2Void provides effective noise reduction in low-field MRI applications, although PSNR improvements (3–6 dB) remain lower than those of supervised models.

The use of MRI phantoms for noise characterization has been investigated in various contexts, however, current evaluations tend to focus on SSIM and PSNR metrics, rarely considering k-space noise statistics. Recent work such as Muckley et al. (2021) [55], demonstrated the effectiveness of k-space processing for the reconstruction of accelerated MRI scans, but did not consider the denoising problem.

Cold Diffusion Models are an innovative direction in image reconstruction, but their main goal is reconstruction from incomplete samples, rather than noise reduction in complete data. Our method, in contrast, is distinguished by the explicit modeling of noise statistics in k-space based on experimental data from phantoms, which provides a physically reliable basis for the denoising process.

Both classical and modern denoising algorithms were used for comparison. Among the traditional methods, Gaussian and Wiener filters were used, which provide basic noise smoothing, but do not take into account the spatial-

correlation structure of the signal. Non-Local Means (NLM) demonstrate higher efficiency [56] and BM3D (*Block-Matching and 3D Filtering*) [57], which remain the benchmark among classical approaches.

In the field of deep learning, DnCNN is most commonly used [38], FFDNet (*Flexible and Fast Denoising CNN*) [58]and RED-CNN [53], which achieve high results due to residual connections and flexible adaptation to different noise levels. Another representative of this class is RCAN (Residual Channel Attention Network), which implements channel attention to improve the recovery of small details [59].

Recent advances in image restoration are related to the use of transformer architectures, in particular SwinIR (Swin Transformer for Image Restoration). [60] and Restormer (Efficient Transformer for High-Resolution Image Restoration) [61], which combine local attention mechanisms with global contextual processing. For MRI signal recovery tasks, NAFNet (Nonlinear Activation Free Network) and recurrent neural approaches for analyzing incomplete FID (Fréchet Inception Distance) signals in MR spectroscopy are also promising [62].

In the context of MRI reconstruction, the VarNet (Variational Network for MRI Reconstruction) model [63] is an example of integrating the physics of signal formation into the reconstruction process, which is consistent with the concept used in our work.

Table 2. Comparison of the proposed method with a number of classical and modern approaches to image denoising.

Method	PSNR (dB)	SSIM	SNR (dB)	EPI	NCC	Time (s)	Complexity
Classical Methods							
Gaussian Filter	28.5	0.65	22.1	3.2	0.82	0.1	Low
Wiener Filter	31.2	0.72	25.8	2.8	0.85	0.2	Low
Non-Local Means	34.1	0.78	28.5	2.1	0.88	15.2	Medium
BM3D	36.8	0.82	31.2	1.9	0.91	8.7	Medium
Deep Learning Methods							
DnCNN	38.2	0.86	32.8	1.7	0.93	2.1	High
FFDNet	41.3	0.9	35.9	1.5	0.95	3.2	High
RED-CNN	39.5	0.88	34.1	1.5	0.94	1.8	High
RCAN	41.1	0.91	36.8	1.6	0.96	4.8	High
State-of-the-Art Methods							
SwinIR	41.2	0.92	39.2	1	0.97	6.1	Very High
Restormer	42.8	0.93	39.9	1.2	0.97	5.3	Very High
NAFNet	43.4	0.94	40.5	1	0.98	7.4	Very High
VarNet	43.5	0.94	40.8	0.8	0.98	7.2	Very High
Proposed (k-space phantom)	44.5 (+1.2)	0.996 (+0.066)	48.4 (+9.2)	0.95 (-0.05)	0.998 (+0.028)	3.2	High

The results show that the proposed model outperforms existing solutions not only in numerical metrics, but also in terms of consistency with the physics of MR signal formation. While classical methods (NLM, BM3D) provide limited contrast improvement, and modern CNN- and Transformer-based approaches (DnCNN, SwinIR, Restormer) focus on statistical texture restoration, the proposed model combines both approaches - physically based noise modeling in k-space and adaptive neural network training, which makes it more versatile for real clinical applications. The model demonstrates the best ratio between noise reduction and anatomical structure preservation, confirming the prospects of physically based architectures in MRI image denoising tasks.

3.3. Limitations and prospects

Despite the achieved results, the proposed approach has some natural, technical and physical limitations inherent in all modern methods of deep denoising of MRI images. At the same time, most of them do not reduce the efficiency of the developed system, but rather outline the directions for its further improvement.

First of all, the current architecture is focused on compensation of stationary noise components, the parameters of which are relatively stable within the slice or series. This is quite justified for most clinical protocols, however, in cases of non-stationary disturbances - for example, artifacts of respiratory or cardiac movements, inter-slice shifts or weak phase decoherence - the efficiency decreases due to a change in the local noise structure. In the future, it is advisable to expand the model by kinematic regularization or motion-aware attention blocks, which will be able to take into account the temporal and spatial correlation between frames, ensuring stability in multiphase or dynamic studies.

An important stage of further verification is testing the model on a wider range of contrasts and different MR systems. This will allow quantitatively confirming the generalizability of the approach. The available results, based on a combination of reference metrics (PSNR, SSIM, NCC, EPI) and ROI-based indicators (SNR, CV), already demonstrate a high correlation between the mathematical quality assessment and the visual reliability of the reconstructed structures, which confirms the practical stability of the model even on data without standards. However, future experiments provide an even deeper assessment of these metrics in the context of quantitative MRI diagnostics, where even minimal deviations in signal levels can affect the biophysical parameters of tissues.

The use of experimentally measured phantom noise statistics requires special attention. This approach ensures the physical reliability of training, since the parameters have a real physical origin. However, these statistics may vary depending on the magnetic field intensity, temperature, coil type, or reconstruction method. Further development in this direction involves distilling statistics directly from clinical images, for example, through Bayesian noise parameter estimation or adaptive learning using pre-trained generative models.

Another promising direction is the integration of the proposed architecture with variational and generative-adversarial models. Such a combination will allow creating more versatile reconstruction systems that are capable not only of suppressing noise, but also of restoring undermeasured or artifactual data, which is especially important for accelerated and undersampled sequences.

Finally, it is planned to evaluate the impact of the model not only on image quality, but also on quantitative MR parameter maps (T1/T2-mapping, ADC, perfusion maps). This will allow us to establish to what extent the improvement in SNR and the reduction in CV after processing translate into an increase in the reliability of the calculated biophysical quantities. Thus, the proposed approach is physically justified, consistent with modern trends in MR analysis, and has the potential for further development in the direction of fully interpretable, statistically adaptive denoising of medical images.

CONCLUSIONS

This paper presents an improved method for denoising MRI images based on modeling noise directly in the frequency domain using statistical characteristics obtained from physical phantoms. This approach provides a more realistic reproduction of the signal generation process and allows to reconcile synthetically generated noise with real clinical imaging conditions. The proposed neural network architecture, which combines residual blocks, CBAM attention mechanisms, ASPP and integration of noise statistics at deep levels, demonstrated improvements in key metrics. In particular, a stable increase in PSNR by 8-10 dB, SSIM close to 1.0, a decrease in MAE and high-quality preservation of fine structural details were observed. All tested images showed consistency of results, which confirms the reproducibility of the algorithm. Comparative results show that our proposed method outperforms both classical approaches and modern deep learning and transform models, providing a stable increase in PSNR by 2-7 dB (Table 2) and almost ideal SSIM/NCC values compared to the best existing solutions.

The evaluation of the model's effectiveness on real clinical MRI images without standards showed that the proposed approach provides a stable improvement in local quality metrics. In particular, the SNR and CV calculated within the ROI demonstrate an average increase in SNR by 6–8% and a decrease in CV within 4–7%, which indicates a reduction in heterogeneity and improved signal uniformity in tissues.

The practical value of the obtained results lies in the possibility of improving the quality of MRI in scenarios where high noise limits diagnostic informativeness. Preservation of structural details and clarity of boundaries can contribute to increasing the accuracy of contouring and treatment planning, as well as reducing the need for repeated scans. This makes the method promising for application in clinical tasks related to diagnostics, therapy planning and patient monitoring.

Further development directions include expanding the phantom database, modeling motion artifacts in k-space, testing on clinical data obtained using multi-scanner systems, and integrating uncertainty assessment methods. All this will make the model even more adaptive and flexible for different imaging scenarios. An additional vector is the use of generative approaches and expanding the training samples with different noise scenarios to increase the generalizability and reliability of the model in practical conditions.

Ethics statement

All clinical data were fully anonymized prior to the study. The use of phantom data and patient images was agreed with the Oberig Medical Center (Kyiv, Ukraine). No additional informed consent was required from patients, as the data did not contain personally identifiable information.

Acknowledgements

We express our sincere gratitude to the Oberig Medical Center (Kyiv, Ukraine) for providing physical phantoms for experiments and anonymized patient images, which made this study possible. We are also grateful to the Taras Shevchenko National University of Kyiv for supporting the scientific work.

Data Availability Statement

The brain MRI dataset utilized in this study was retrospectively collected at Oberig Medical Center and has been fully anonymized to protect patient confidentiality. Due to the institutional data governance policies and ethical restrictions, the raw dataset is not publicly available. However, the anonymized data can be made available to qualified researchers for non-commercial, academic purposes upon reasonable request to the corresponding author.

ORCID

D.G. Sliusarenko, https://orcid.org/0009-0009-1802-5859, **A.V. Netreba,** https://orcid.org/0000-0003-1347-3854

REFERENCES

[1] Z. Chen, K. Pawar, M. Ekanayake, C. Pain, S. Zhong, and G.F. Egan, J. Digit. Imaging, **36**, 204 (2023). https://doi.org/10.1007/s10278-022-00721-9

[2] J.I. Tamir, M. Blumenthal, J. Wang, T. Oved, E. Shimron, and M. Zaiss, Magn. Reson. Mater. Phys. Biol. Med. **38**, 367 (2025). https://doi.org/10.1007/s10334-025-01236-4
[3] T. Ssentamu, A. Kimbowa, R. Omoding, E. Atamba, P.K. Mukwaya, G.W. Jjuuko, and S. Geethanath, Front. Neuroimaging, **4**, (2025). https://doi.org/10.3389/fnimg.2025.1501801
[4] A. Salehi, M. Mach, C. Najac, B. Lena, T. O'Reilly, Y. Dong, P. Börnert, *et al*., J. Magn. Reson. **370**, 107812 (2025). https://doi.org/10.1016/j.jmr.2024.107812
[5] P. Song, J. Xu, X. Liu, Z. Zhang, X. Rao, R.P. Martinho, Q. Bao, and C. Liu, J. Magn. Reson. **359**, 107615 (2024). https://doi.org/10.1016/j.jmr.2023.107615
[6] D. Koprivica, R.P. Martinho, M. Novakovic, M.J. Jaroszewicz, and L. Frydman, J. Magn. Reson. **338**, 107187 (2022). https://doi.org/10.1016/j.jmr.2022.107187
[7] Y. Zhang, W. He, F. Chen, J. Wu, Y. He, and Z. Xu, J. Magn. Reson. **344**, 107319 (2022). https://doi.org/10.1016/j.jmr.2022.107319
[8] D. Singh, A. Monga, H.L. de Moura, X. Zhang, M.V.W. Zibetti, and R.R. Regatte, Bioeng. Basel Switz. **10**, 1012 (2023). https://doi.org/10.3390/bioengineering10091012
[9] M. Jiang, S. Wang, K.-H. Chan, Y. Sun, Y. Xu, Z. Zhang, Q. Gao, *et al*., Comput. Med. Imaging Graph. Off. J. Comput. Med. Imaging Soc. **121**, 102497 (2025). https://doi.org/10.1016/j.compmedimag.2025.102497
[10] B. Kang, W. Lee, H. Seo, H.-Y. Heo, and H. Park, Magn. Reson. Med. **92**, 1980 (2024). https://doi.org/10.1002/mrm.30197
[11] M.A. Sultan, C. Chen, Y. Liu, K. Gil, K. Zareba, and R. Ahmad, Magn. Reson. Mater. Phys. Biol. Med. **38**, 859 (2025). https://doi.org/10.1007/s10334-025-01257-z
[12] Q. Tian, Z. Li, Q. Fan, J.R. Polimeni, B. Bilgic, D.H. Salat, and S.Y. Huang, NeuroImage, **253**, 119033 (2022). https://doi.org/10.1016/j.neuroimage.2022.119033
[13] E.D. Hussner, S. Sundby, C.B. Outzen, J. Jensen, A. Tingberg, and H. Precht, J. Med. Imaging Radiat. Sci. **56**, 101814 (2025). https://doi.org/10.1016/j.jmir.2024.101814
[14] S. Kojima, T. Ito, and T. Hayashi, J. Med. Phys. **47**, 387 (2022). https://doi.org/10.4103/jmp.jmp_71_22
[15] S.M.A. Sharif, R.A. Naqvi, and W.-K. Loh, IEEE Trans. Radiat. Plasma Med. Sci. **8**, 521 (2024). https://doi.org/10.1109/TRPMS.2024.3380090
[16] K.V. Jordanova, S.E. Russek, and K.E. Keenan, Magn. Reson. Mater. Phys. Biol. Med. **38**, 727 (2025). https://doi.org/10.1007/s10334-025-01270-2
[17] K.E. Keenan, K.V. Jordanova, S.E. Ogier, D. Tamada, N. Bruhwiler, J. Starekova, J. Riek, *et al*., Magn. Reson. Mater. Phys. Biol. Med. **37**, 535 (2024). https://doi.org/10.1007/s10334-024-01181-8
[18] K.E. Keenan, M. Ainslie, A.J. Barker, M.A. Boss, K.M. Cecil, C. Charles, T.L. Chenevert, *et al*., Magn. Reson. Med. **79**, 48 (2018). https://doi.org/10.1002/mrm.26982
[19] C.P. Cheng, and Y.O. Halchenko, F1000Research, **9**, 1131 (2020). https://doi.org/10.12688/f1000research.24544.1
[20] R.W. Brown, Y.-C.N. Cheng, E.M. Haacke, M.R. Thompson, and R. Venkatesan, *Magnetic Resonance Imaging: Physical Principles and Sequence Design*, (John Wiley & Sons, 2014).
[21] W.A. Edelstein, G.H. Glover, C.J. Hardy, and R.W. Redington, Magn. Reson. Med. **3**, 604 (1986). https://doi.org/10.1002/mrm.1910030413
[22] H. Gudbjartsson and S. Patz, Magn. Reson. Med. **34**, 910 (1995). https://doi.org/10.1002/mrm.1910340618
[23] N. Just, Br. J. Cancer **111**, 2205 (2014). https://doi.org/10.1038/bjc.2014.512
[24] G. Vegas-Sánchez-Ferrero, M.J. Ledesma-Carbayo, G.R. Washko, and R.S.J. Estépar, Med. Image Anal. **40**, 44 (2017). https://doi.org/10.1016/j.media.2017.06.001
[25] H. Liu, Z. Li, S. Lin, and L. Cheng, Sensors, **23**, 7044 (2023). https://doi.org/10.3390/s23167044
[26] L.-C. Chen, G. Papandreou, F. Schroff, and H. Adam, (2017). https://doi.org/10.48550/arXiv.1706.05587
[27] E. Perez, F. Strub, H. de Vries, V. Dumoulin, and A. Courville, in: *Proc. Thirty-Second AAAI Conf. Artif. Intell. Thirtieth Innov. Appl. Artif. Intell. Conf. Eighth AAAI Symp. Educ. Adv. Artif. Intell*, (AAAI Press, New Orleans, Louisiana, USA, 2018), pp. 3942-3951. https://doi.org/10.48550/arXiv.1709.07871
[28] C. Bregler, in: *2015 IEEE Conf. Comput. Vis. Pattern Recognit. CVPR*, (2015). https://doi.org/10.1109/CVPR.2015.7298664
[29] A.L. Maas, in: *Rectifier Nonlinearities Improve Neural Network Acoustic Models*, (2013). https://api.semanticscholar.org/CorpusID:16489696
[30] S. Woo, J. Park, J.-Y. Lee, and I.S. Kweon, ArXiv preprint, (2018), pp. 3–19. https://doi.org/10.48550/arXiv.1807.06521
[31] J. Hu, L. Shen, and G. Sun, ArXiv preprint, ArXiv preprint, (2018), pp. 7132–7141. https://https://doi.org/10.48550/arXiv.1709.01507
[32] B. Yaman, S.A.H. Hosseini, S. Moeller, J. Ellermann, K. Uğurbil, and M. Akçakaya, Magn. Reson. Med. **84**, 3172 (2020). https://doi.org/10.1002/mrm.28378
[33] L. Zhang, M. Wu, L. Wang, D.C. Steffens, G.G. Potter, and M. Liu, ArXiv preprint, (2024). https://doi.org/10.48550/arXiv.2403.08162
[34] H. Chen, Y. Zhang, W. Zhang, P. Liao, K. Li, J. Zhou, and G. Wang, ArXiv preprint, (2016). https://doi.org/10.48550/arXiv.1609.08508
[35] S. Gou, W. Liu, C. Jiao, H. Liu, Y. Gu, X. Zhang, J. Lee, and L. Jiao, Phys. Med. Biol. **64**, 165017 (2019). https://doi.org/10.1088/1361-6560/ab325e
[36] K. He, X. Zhang, S. Ren, and J. Sun, in: *2015 IEEE International Conference on Computer Vision (ICCV)*, (Santiago, Chile, 2015). https://doi.org/10.1109/ICCV.2015.123
[37] A. Horé and D. Ziou, in: *2010 20th Int. Conf. Pattern Recognit*. (2010), pp. 2366–2369. https://doi.org/10.1109/ICPR.2010.579
[38] K. Zhang, W. Zuo, Y. Chen, D. Meng, and L. Zhang, IEEE Trans. Image Process. **26**, 3142 (2017). https://doi.org/10.1109/TIP.2017.2662206
[39] G.P. Renieblas, A.T. Nogués, A.M. González, N. Gómez-Leon, and E.G. del Castillo, J. Med. Imaging, **4**, 035501 (2017). https://doi.org/10.1117/1.JMI.4.3.035501

[40] P. Jain, and V. Tyagi, Inf. Syst. Front. **18**, 159–170 (2016). https://doi.org/10.1007/s10796-014-9527-0
[41] K. P.g., J. Joseph, and S.J., Biocybern, Biomed. Eng. **37**, 159 (2017). https://doi.org/10.1016/j.bbe.2016.12.008
[42] J. Lewis, Vision Interface, **10**(1), 120-123 (1995). https://www.bibsonomy.org/bibtex/232f4a4901ce85a2b37f806ba675c8a0
[43] F.L. Goerner and G.D. Clarke, Med. Phys. **38**, 5049 (2011). https://doi.org/10.1118/1.3618730
[44] E. Alizadeh, Data Sci. (2023). https://towardsdatascience.com/dispersion-cv-qcd-32849f828434/
[45] Z. Jalilibal, A. Amiri, P. Castagliola, and M.B.C. Khoo, Comput. Ind. Eng. **161**, 107600 (2021). https://doi.org/10.1016/j.cie.2021.107600
[46] M. Kidoh, K. Shinoda, M. Kitajima, K. Isogawa, M. Nambu, H. Uetani, K. Morita, *et al.*, Magn. Reson. Med. Sci. **19**, 195 (2019). https://doi.org/10.2463/mrms.mp.2019-0018
[47] N. Nazir, A. Sarwar, and B.S. Saini, Micron, **180**, 103615 (2024). https://doi.org/10.1016/j.micron.2024.103615
[48] H.M.S.S. Herath, H.M.K.K.M.B. Herath, N. Madusanka, and B.-I. Lee, J. Imaging, **11**, 100 (2025). https://doi.org/10.3390/jimaging11040100
[49] J. Joseph, S. Jayaraman, R. Periyasamy, and S.V. Renuka, Curr. Med. Imaging, **13**, 58 (2017). https://doi.org/10.2174/1573405612666160609131149
[50] K. Ohashi, Y. Nagatani, M. Yoshigoe, K. Iwai, K. Tsuchiya, A. Hino, Y. Kida, *et al.*, J. Digit. Imaging, **36**, 2623 (2023). https://doi.org/10.1007/s10278-023-00875-0
[51] D. Sliusarenko, A. Netreba, and S. Radchenko, in: *2024 IEEE 42nd Int. Conf. Electron. Nanotechnol. ELNANO*, (2024), pp. 456–460. https://doi.org/10.1109/ELNANO63394.2024.10756858
[52] K. Usui, K. Ogawa, M. Goto, Y. Sakano, S. Kyougoku, and H. Daida, Vis. Comput. Ind. Biomed. Art **4**, 21 (2021). https://doi.org/10.1186/s42492-021-00087-9
[53] A. Ferdi, S. Benierbah, and A. Nakib, Multimed. Tools Appl. **84**, 21625 (2025). https://doi.org/10.1007/s11042-024-20175-1
[54] Z. Wang, J. Chen, and S.C.H. Hoi, ArXiv preprint, (2020). https://doi.org/10.48550/arXiv.1902.06068
[55] M.J. Muckley, B. Riemenschneider, A. Radmanesh, S. Kim, G. Jeong, J. Ko, Y. Jun, *et al.*, IEEE Trans. Med. Imaging, **40**, 2306 (2021). https://doi.org/10.1109/TMI.2021.3075856
[56] A. Buades, B. Coll, and J.-M. Morel, in: *2005 IEEE Comput. Soc. Conf. Comput. Vis. Pattern Recognit. CVPR05*, (2005), pp. 60–65 vol. 2. https://doi.org/10.1109/CVPR.2005.38
[57] K. Dabov, A. Foi, V. Katkovnik, and K. Egiazarian, IEEE Trans. Image Process. **16**, 2080 (2007). https://doi.org/10.1109/TIP.2007.901238
[58] K. Zhang, W. Zuo, and L. Zhang, IEEE Trans. Image Process. **27**, 4608 (2018). https://doi.org/10.1109/TIP.2018.2839891
[59] Y. Zhang, K. Li, K. Li, L. Wang, B. Zhong, and Y. Fu, in: *Comput. Vis. – ECCV 2018 15th Eur. Conf. Proc*. Part VII (Springer-Verlag, Berlin, Heidelberg, 2018), pp. 294–310. https://doi.org/10.1007/978-3-030-01234-2_18
[60] J. Liang, J. Cao, G. Sun, K. Zhang, L.V. Gool, and R. Timofte, ArXiv preprint, (2021). https://doi.org/10.48550/arXiv.2108.10257
[61] S.W. Zamir, A. Arora, S. Khan, M. Hayat, F.S. Khan, and M.-H. Yang, ArXiv preprint, (2022). https://doi.org/10.48550/arXiv.2111.09881
[62] E. Jeong, J. Jang, J. Kim, and H. Kim, J. Magn. Reson. **368**, 107762 (2024). https://doi.org/10.1016/j.jmr.2024.107762
[63] C. Millard and M. Chiew, Bioengineering, **11**, 1305 (2024). https://doi.org/10.3390/bioengineering11121305

ШУМОЗАГЛУШЕННЯ МРТ НА ОСНОВІ ГЛИБОКОГО НАВЧАННЯ З ВИКОРИСТАННЯМ СТАТИСТИКИ ШУМУ, ОТРИМАНОЇ З ВИМІРЮВАНЬ ФІЗИЧНИХ ФАНТОМІВ

Д.Г. Слюсаренко[1,2], А.В. Нетреба[1]

[1]Факультет радіофізики, електроніки та комп'ютерних систем, Київський національний університет імені Тараса Шевченка, вул. Володимирська, 64/13, Київ, Україна, 01601

[2]Національний інститут раку України, вул. Юлія Здановського, 33/43, Київ, Україна, 03022

Високоякісні МРТ-зображення є важливими для точного визначення об'ємів-мішеней та органів, що знаходяться в групі ризику, а також для правильної реєстрації на КТ під час планування променевої терапії. Метою цієї роботи є розробка надійного методу шумозаглушення, який покращує візуалізацію структур мозку та зберігає анатомічні деталі. Запропоновано модель, засновану на модифікованій архітектурі U-Net із залишковими блоками, модулями уваги (CBAM) та просторовим пірамідальним об'єднанням. Підхід характеризується інтеграцією статистичних шумових характеристик, отриманих з фантомних вимірювань, та моделюванням деградацій у псевдо-k-просторі (включаючи розподіли гаусового та релеївського шуму). Валідацію було проведено на 1000 анонімізованих клінічних DICOM-зображеннях зі змінними рівнями шуму. Запропонована модель забезпечила збільшення PSNR на 8–10 дБ та збільшення SSIM з 0,72 до 0,97. Індекс збереження країв (EPI), який досяг значень 8,0 на шумних зображеннях через артефакти, стабілізувався на рівні 1,0 після обробки, що свідчить про ефективне видалення псевдоконтурів без розмиття справжніх анатомічних меж. Крім того, на реальних зображеннях спостерігалося середнє покращення SNR на 7% та зниження CV на 4–7%, що підтверджує стабільність методу. Поєднання фізично обґрунтованого моделювання шуму в частотній області та сучасних архітектур глибокого навчання дозволяє ефективно видаляти шум, зберігаючи при цьому критичні анатомічні межі. Метод має високий потенціал для клінічного впровадження в процедурах планування променевої терапії, зокрема для підвищення точності об'єднання МРТ/КТ.

Ключові слова: *шумозаглушення МРТ, моделювання шуму в k-просторі, глибоке навчання, адаптивне масштабування шуму, моделювання в області Фур'є, реконструкція медичних зображень, CNN*